Supporting Information

$MoSe_2$/SWNT core–shell hybrids with space-charge-limited conduction and nonlinear dynamics for in-materio reservoir computing

Alif Syafiq Kamarol Zaman[1], Saman Azhari[2,3], Muzhen Xu[3], Yuki Usami[1,3], and Hirofumi Tanaka[1,3,*]

[1]Graduate School of Life Science and Systems Engineering, Kyushu Institute of Technology, 2-4 Hibikino, Wakamatsu, Kitakyushu, 808-0196 Japan.

[2]Graduate School of Information, Production and Systems (IPS), Waseda University, 2-7 Hibikino, Wakamatsu, Kitakyushu, 808-0135 Japan.

[3]Research Center for Neuromorphic AI Hardware, Kyushu Institute of Technology, 2-4 Hibikino, Wakamatsu, Kitakyushu, 808-0196 Japan.

*Corresponding Author: tanaka@brain.kyutech.ac.jp

S1. Fabrication of a 16-electrode device

S1.1. Electrode patterning

The 16-electrode device was fabricated on a silicon/silicon dioxide (Si/SiO_2) substrate. The device consists of 16 square aluminum (Al) electrodes arranged in a pattern (as shown in **Figure 1**), with a maximum opposing gap size of 100 μm. The electrodes were patterned using a standard photolithography and lift-off process. This process begins with substrate cleaning, in which the Si/SiO_2 substrate was sequentially cleaned in an ultrasonic bath of isopropyl alcohol (IPA) and DI water, each for 3 minutes, and then dried. Then, the resist was coated, in which a bi-layer resist was prepared for the lift-off process. First, a lift-off resist (LOR-10A) was spin-coated onto the substrate at 3,000 rpm for 50 s and baked on a hot plate at 180 °C for 5 minutes. Subsequently, a photoresist (S18186) was spin-coated on top at 4,000 rpm for 2 s and baked at 90 °C for 3 minutes. After this patterning was achieved by using a chromium photomask with the electrode pattern placed over the substrate. The device was then exposed to UV light for 10 s at an intensity of 19 mW/cm^2 using a mask aligner. The exposed resist was developed in an MF-319 developer for 90 s, rinsed with DI water, and hard-baked at 120 °C for 5 minutes to define the pattern. Then, metallization and lift-off were performed, in which a 50 nm layer of aluminum (Al**)** was deposited over the substrate via sputtering at a base pressure of 10^{-5} Torr. The lift-off was then performed by submerging the substrate in a dimethyl sulfoxide (DMSO) bath at 60 °C for 30 minutes. This step dissolves the underlying LOR and removes the excess metal. Finally, the completed electrode array was rinsed with IPA and DI water and dried, resulting in the patterned device.

S1.2. Material Deposition and Device Packaging

The synthesized $MoSe_2$/SWNT composite powder (with SWNT loadings of 1, 5, and 10 mg) was dispersed in ethanol to create a suspension with a concentration of 40 mg/mL. The suspension was

then homogenized via ultrasonication for 10 minutes. The active material was deposited by drop-casting three 1 μL drops (approximately 3 μL total volume) from a micropipette onto the central 100 μm gap of the electrode array. During this process, the substrate was held on a hot plate at 70 °C to facilitate controlled solvent evaporation. After the material was fully dried, the Si/SiO_2 chip was mounted onto a custom-designed printed circuit board (PCB). Electrical connections from the 16 aluminum electrode pads to the corresponding PCB contacts were then established using silver paste for wire bonding. The fully packaged device was then ready for electrical characterization and reservoir computing experiments.

S2. FFT Analysis and High-Dimensional Representation

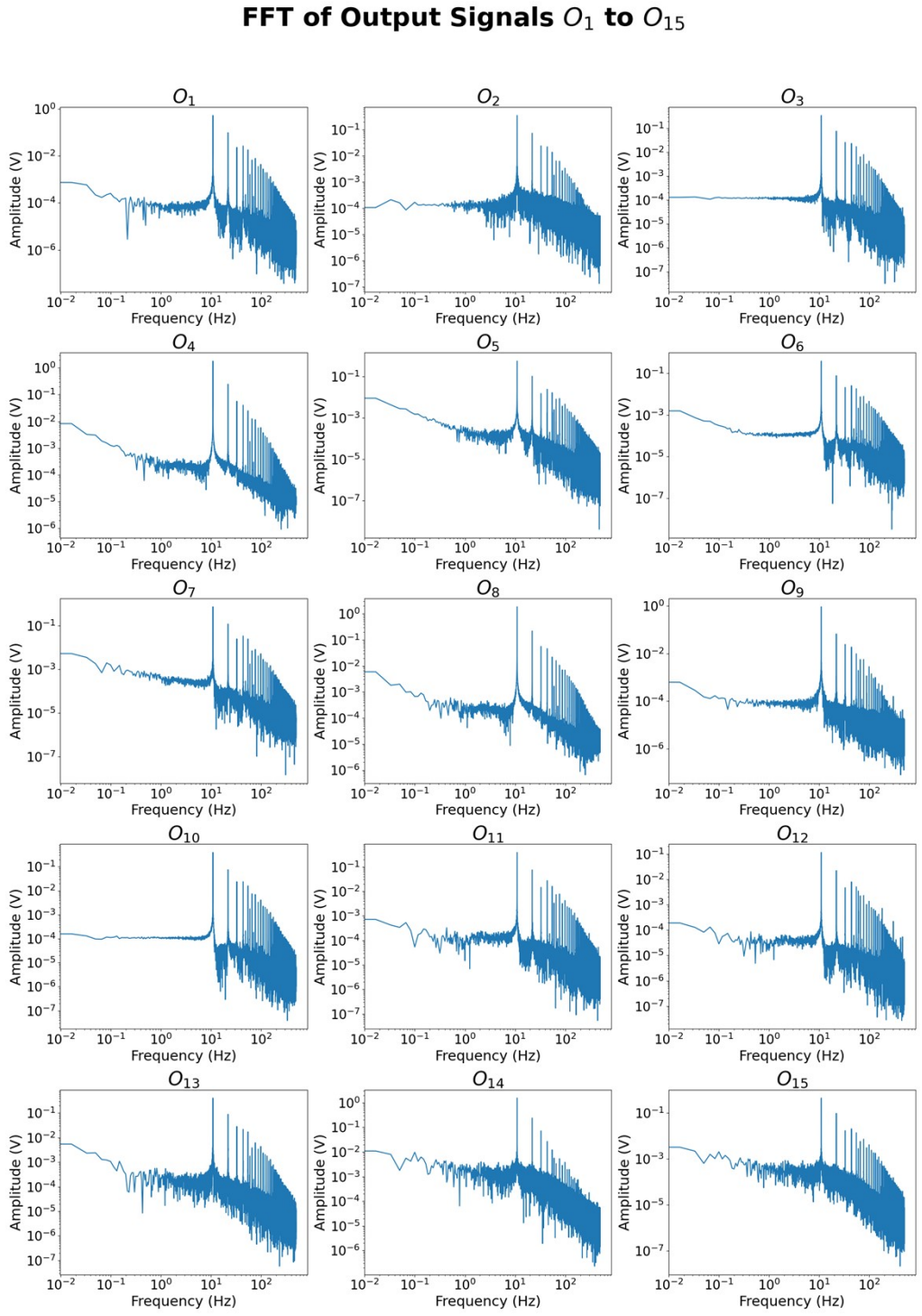

Figure S1. FFT amplitude spectra of the 15 device output signals O_1 to O_{15} obtained under an 11 Hz sinusoidal input voltage. The spectra exhibit pronounced peaks at the fundamental frequency of 11 Hz and at higher harmonic frequencies such as 22 Hz and 33 Hz. The generation of these integer multiples confirms the nonlinear dynamical response of the $MoSe_2$/SWNT reservoir.

FFT analysis of the device outputs clearly shows pronounced peaks at the fundamental and harmonic frequencies as shown in **Figure S2**. By feeding a sine wave with a fundamental frequency of 11 Hz into the device, we observed its output through FFT analysis which revealed the presence of harmonics at integer multiples of the input frequency such as 22 Hz and 33 Hz. This harmonic generation indicates nonlinearity in the device response which is a desirable characteristic for effective reservoir computing[3–5]. The raw input and output signals used for this analysis are provided in **Figure S4.** Across the output signals (O_1 to O_{15}), significant peaks appear at the fundamental frequency and its harmonics, which aligns with the device's demonstrated ability to generate accurate representations of complex waveforms. The amplitude spectrum reveals a concentration of energy at harmonic frequencies, indicating that the device is introducing nonlinear transformations to the input signals. These transformations, driven by the device's nonlinear behavior, are critical for mapping the input signals into a higher-dimensional space. In the context of waveform reconstruction, this harmonic content is particularly important. For instance, the successful regression results for waveforms such as the triangle and square waves, which are rich in harmonic content, are reflected in the pronounced harmonic peaks in the FFT plots. This suggests that the device can capture the essential harmonic components that define these waveforms, further confirming its role as a nonlinear reservoir. The FFT analysis also provides insight into the device's ability to handle signals composed of higher-order harmonics, such as Sin2ω and Sin3ω. While higher harmonics typically introduce more spectral complexity, the device demonstrated strong regression performance for both cases. Notably, in the Sin3ω case, where more complex harmonic content is present, the FFT plots still reveal well-defined peaks with limited degradation in harmonic amplitude. This is consistent with the observed regression accuracy of 95.1%, indicating that the device maintains sufficient precision even at higher

harmonic orders. Overall, the FFT results support the conclusion that the device not only transforms input signals nonlinearly but does so in a way that retains essential spectral features critical for accurate waveform reconstruction.

S3. Lissajous Plots and Nonlinear Dynamics

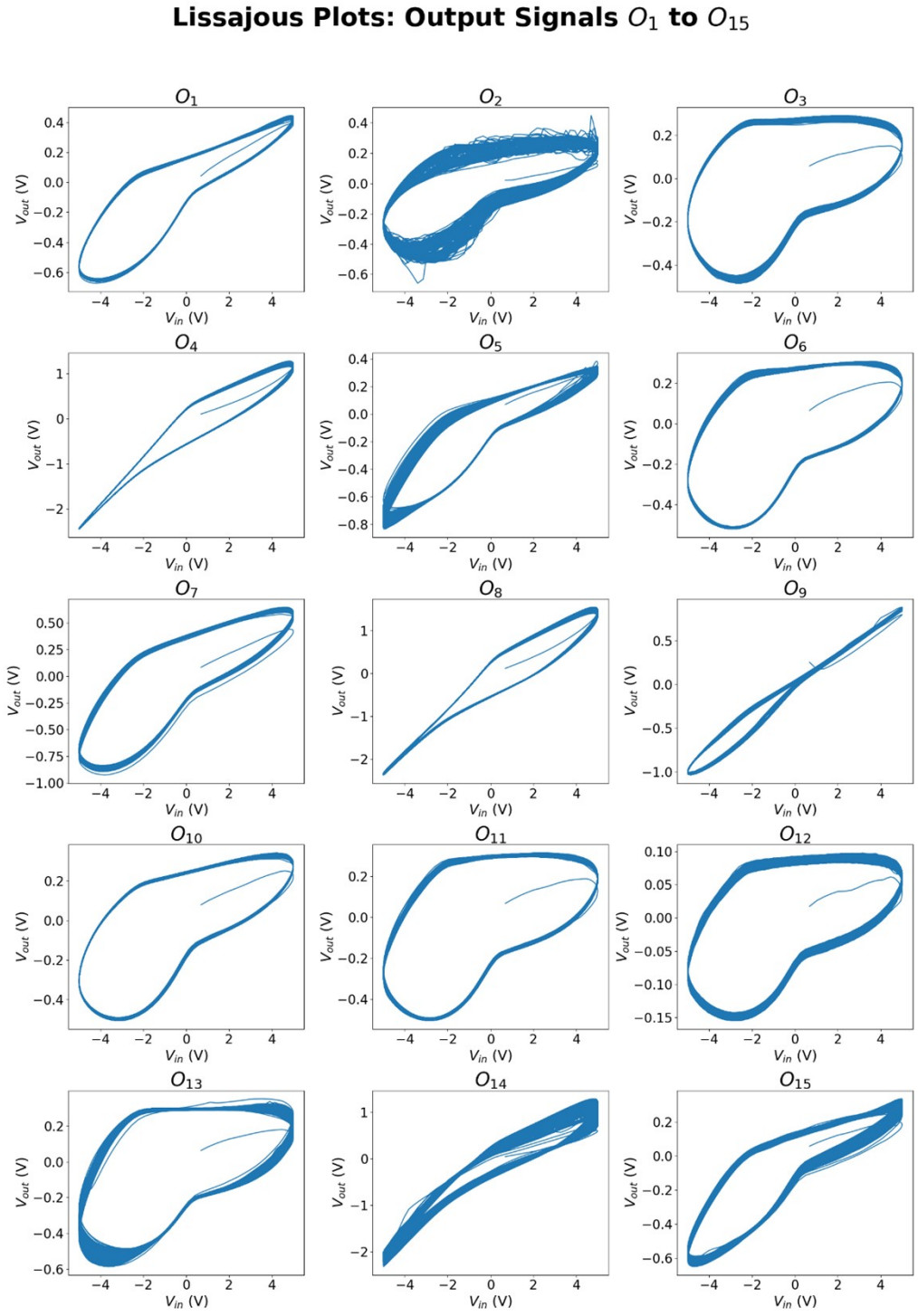

Figure S2. Lissajous plots of all 15 outputs from the device showing asymmetric and hysteresis shape suggesting rich non-linearity and phase shifts

The Lissajous plots, depicted in the attached figures, provide a clear visualization of the nonlinear relationship between the input and output signals of the $MoSe_2$/SWNT core-shell device. These plots were generated by plotting the output voltage (V_{out}) against the input voltage (V_{in}) for each of the device's output channels (O_1 to O_{15}) as shown in **Figure S3**. The resulting shapes, predominantly asymmetrical ellipses, are indicative of phase shifts and nonlinear dynamics introduced by the device. The elliptical shapes seen in the Lissajous plots typically emerge when the input and output signals share the same frequency, but the asymmetry of these ellipses reveals that the device is introducing significant phase shifts and nonlinear transformations to the input signal. This is a direct consequence of the nonlinearities in the device, which are essential for the reservoir computing framework. Nonlinear transformations enrich the dynamics of the system, enabling the reservoir to map input signals into a high-dimensional space, facilitating the separation and classification of complex patterns.

The Lissajous plots vary across different output signals, with some displaying more pronounced asymmetry (e.g., O_2, O_5, O_{11}) while others exhibit tighter, more elliptical shapes. These variations reflect the device's ability to apply different degrees of phase shifts and nonlinear modifications depending on the specific output channel. For example, output O_2 shows a highly irregular and overlapping Lissajous figure, suggesting that the device has introduced a significant nonlinear distortion to the input. In contrast, outputs like O_1 and O_3 maintain a clearer elliptical shape with slight asymmetry, indicating more moderate nonlinear transformations.

These asymmetrical elliptical shapes are critical for reservoir computing applications. The nonlinearity they represent ensures that the input signal is transformed into a rich, high-dimensional representation, which is necessary for the system to perform tasks such as pattern recognition and time-series prediction. The phase shifts alter the orientation and size of the

Lissajous figures, further emphasizing the device's capability to introduce complex dynamics. These dynamics, captured in the Lissajous plots, provide a visual confirmation of the nonlinear behavior observed in both the FFT analysis and waveform reconstruction tasks discussed previously.

S4. Total harmonic distortion

Total Harmonic Distortion (THD) is another metric for quantifying the nonlinearity of a reservoir computing system, particularly in physical implementations where the reservoir transformation is governed by material properties[1,2]. In an ideal linear system, a pure sinusoidal input should only contain its fundamental frequency. However, a nonlinear system such as a memristive reservoir naturally generates higher harmonics at integer multiples of the input frequency. The degree of harmonic generation is quantified by THD, defined as:

$$THD = \frac{\sqrt{A_2^2 + A_3^2 + A_4^2 + \ldots + A_{15}^2}}{A_1} \#(11)$$

where A_1 is the amplitude of the fundamental frequency, and $[A_2, A_3, A_4, \ldots, A_{15}]$ represent the amplitudes of the harmonic components. In the context of waveform reconstruction, THD provides insight into how the reservoir expands the input signal into a richer feature space, enabling the readout layer to synthesize complex waveforms from a single sinusoidal input. This is linked to Fourier series decomposition, where any periodic function can be represented as a sum of sinusoids at different frequencies. Since many target waveforms (e.g., triangle, square, and sawtooth waves) require specific harmonic components as from equations (12) – (15), the ability of the reservoir to generate these harmonics is crucial for achieving high reconstruction accuracy. Figure S3 presents the measured THD across the 15 output electrodes, revealing a heterogeneous nonlinearity distribution with values spanning from 8.0% O_9 to 24.7% O_3. This variation indicates that different nodes within the reservoir provide diverse harmonic components, rather than a uniform transformation. By correlating THD with waveform reconstruction performance, as shown in **Figure S3**, we demonstrate that the memristive reservoir not only exhibits strong nonlinear

transformation capabilities but also provides an effective basis for encoding diverse time-series signals.

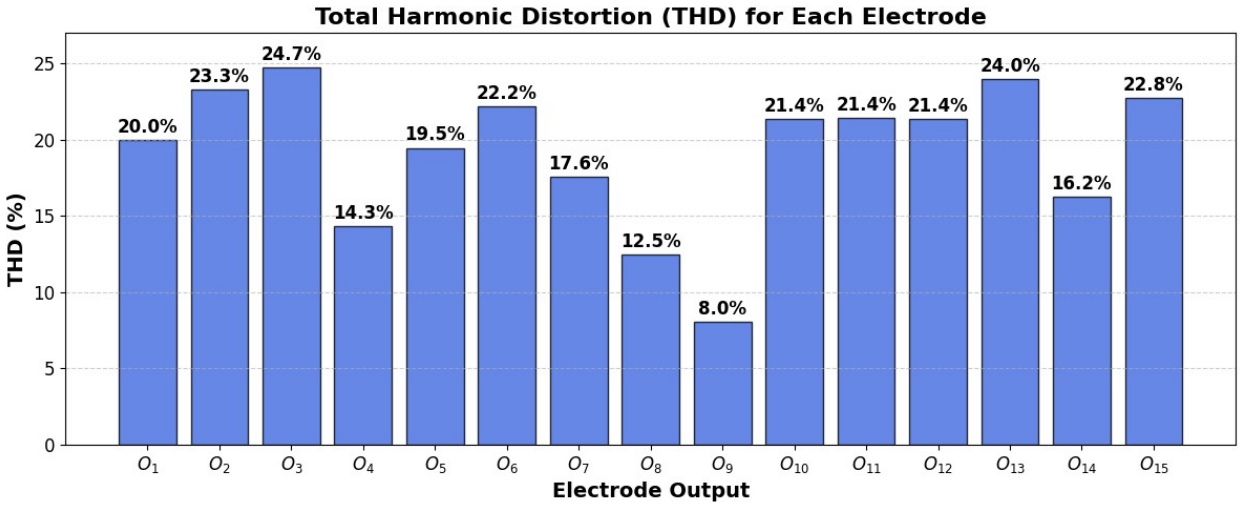

Figure S3. Total harmonic distortion of all 15 outputs of the reservoir.

$$Cosine\ wave = f(x) = sin\left(\frac{\pi}{2} - x\right) \#(12)$$

$$Triangle\ wave = f(x) = \frac{8}{\pi^2} \sum_{i=1,3,5,\ldots}^{\infty} \frac{(-1)^{\frac{n-1}{2}}}{n^2} sin\left(\frac{n\pi x}{L}\right) \#(13)$$

$$Sawtooth\ wave = f(x) = \frac{1}{2} - \frac{1}{\pi} \sum_{i=1}^{\infty} \frac{1}{n} sin\left(\frac{n\pi x}{L}\right) \#(14)$$

$$Square\ wave = f(x) = \frac{4}{\pi} \sum_{i=1,3,5,\ldots}^{\infty} \frac{1}{n} sin\left(\frac{n\pi x}{L}\right) \#(15)$$

S5. Input and Output representations of benchmark tasks

The input and output of waveform reconstruction tasks is 11 Hz sine wave as shown in **Figure S4**. We observed one of the outputs of their reservoir is a little bit distorted, an indication of the nonlinear transformation by the reservoir on the input signal.

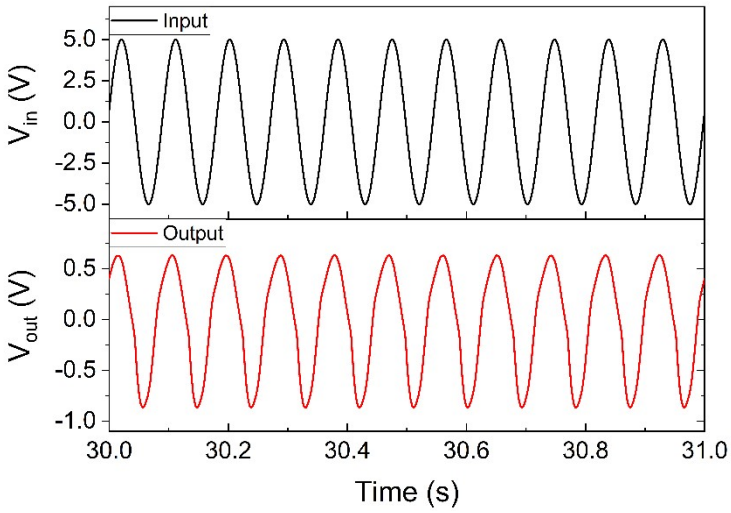

140

141 **Figure S4**. Input and output representation of waveform reconstruction task.

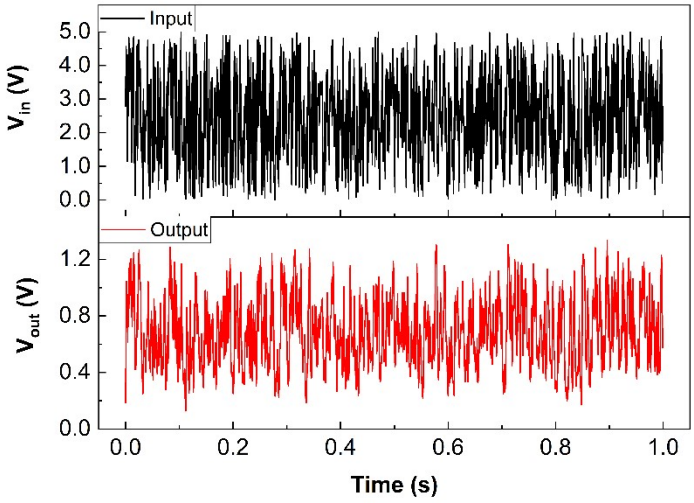

142

143 **Figure S5.** Input and output representation of NARMA2 and MC task.

144

References

1 A. Arranz-Gimon, A. Zorita-Lamadrid, D. Morinigo-Sotelo and O. Duque-Perez, *Energies 2021, Vol. 14, Page 6467*, 2021, 14, 6467.

2 D. Shmilovitz, *IEEE Transactions on Power Delivery*, 2005, 20, 526–528.

3 O. Srikimkaew, D. Banerjee, S. Azhari, Y. Usami and H. Tanaka, *ACS Appl Electron Mater*, 2024, 6, 688–695.

4 D. Banerjee, T. Kotooka, S. Azhari, Y. Usami, T. Ogawa, J. K. Gimzewski, H. Tamukoh and H. Tanaka, *Advanced Intelligent Systems*, 2022, 4, 2100145.

5 G. Abdi, A. Karacali, A. S. K. Zaman, M. Gryl, A. Sławek, A. Szkudlarek, H. Tanaka and K. Szaciłowski, *Adv Electron Mater*, DOI:10.1002/aelm.202500049.